

# Digital logic gates in soft, conductive mechanical metamaterials

Charles El Helou<sup>1</sup>, Philip R. Buskohl<sup>2</sup>, Christopher E. Tabor<sup>2</sup> & Ryan L. Harne<sup>1</sup>  

Integrated circuits utilize networked logic gates to compute Boolean logic operations that are the foundation of modern computation and electronics. With the emergence of flexible electronic materials and devices, an opportunity exists to formulate digital logic from compliant, conductive materials. Here, we introduce a general method of leveraging cellular, mechanical metamaterials composed of conductive polymers to realize all digital logic gates and gate assemblies. We establish a method for applying conductive polymer networks to metamaterial constituents and correlate mechanical buckling modes with network connectivity. With this foundation, each of the conventional logic gates is realized in an equivalent mechanical metamaterial, leading to soft, conductive matter that thinks about applied mechanical stress. These findings may advance the growing fields of soft robotics and smart mechanical matter, and may be leveraged across length scales and physics.

<sup>1</sup>Department of Mechanical Engineering, The Pennsylvania State University, University Park, PA, USA. <sup>2</sup>Materials and Manufacturing Directorate, Air Force Research Laboratory, Wright-Patterson Air Force Base, OH, USA. ✉email: [ryanharne@psu.edu](mailto:ryanharne@psu.edu)

Structurally and materially compliant integrated circuits with reconfigurable electrical functions are an essential foundation for human-machine interfaces, soft robotics, and other future electronics that will serve medicine, science, engineering, and industry. These compliant conductors alleviate concerns of failure traditionally encountered when conventional metallic conductors are subjected to mechanical stress<sup>1–5</sup>. Liquid metal is often leveraged in compliant integrated circuits for the high conductivity and reversible self-healing behavior realized by liquid metal-based circuit interconnects<sup>6–8</sup>. Two-phase materials that combine conductive microparticles with a polymer substrate also support electrical function when subjected to large strains, while moreover being amenable to diverse fabrication practices<sup>9–12</sup>. To design the substrate for reconfiguration of a compliant integrated circuit, programmable mechanical deformation is often a candidate for reversible shape change<sup>3,4</sup>. For instance, kirigami<sup>13</sup> and origami<sup>14</sup> have inspired substrates that fold to tailor electrical behavior<sup>15</sup>. Elastic instabilities are also considered to transition electrical states in response to mechanical<sup>16</sup> and thermal<sup>17</sup> stresses.

Reconfiguration of electrical networks is indeed the basis of digital logic, which is integral for information processing in modern computers as well as in the human brain<sup>18</sup>. The search for logic-based information processing in artificial materials has led to concepts of discrete transmittance outputs resulting from elastic wave logic operations in mechanical metamaterials<sup>19</sup> and from infrared wave logic operations in photonic metamaterials<sup>20</sup>. Logic functions in soft matter have also been emulated by high contrast colorimetric outputs from thermochromic elastomers subjected to input pressure states<sup>21</sup>.

Recent progress on embodiments of mechanologic provide another modality of information processing in soft matter. By the concept of mechanologic, a digital bit is abstracted as a reversible, mechanical, or material configuration<sup>22,23</sup>. Recently, discrete shape reconfigurations are cultivated by elastic beam buckling<sup>24,25</sup>. In formulations of buckling-based mechanologic, the two statically stable configurations represent the physical abstraction of discrete digital bits. Together, the digitized bits associated with mechanical buckling modes facilitate logic operations according to the design and assembly of the switchable constituents<sup>26</sup>. This stratagem has been shown for mechanically<sup>27</sup>, chemically<sup>28</sup>, and humidity<sup>29</sup> triggered elastic instabilities. Controller signaling for pressurized soft robots has also been demonstrated through mechanologic-based signal processing, suggesting one means for soft matter autonomy<sup>30</sup>. Yet, current embodiments of logic processing of mechanical stress inputs lack digital electrical outputs, which limits means to communicate with actuation and sensory mechanisms that may require electrical feedback to function<sup>26,27</sup>. Similar to anatomical realizations of intelligence and information processing to monitor

and transmit sensory and motor impulses<sup>31</sup>, a means to cultivate decision-making capability in mechanically-robust compliant materials would provide a significant step towards autonomous soft matter able to assess and react to mechanical-electrical stimuli in a dynamic environment.

This report introduces a class of soft, conductive mechanical metamaterials with programmable elastic instabilities that function as electronic logic gates able to perform digital computations on mechanical stress input combinations. Here, we exploit reversible compact-to-deployed state transitions in conductive mechanical metamaterials through a strategic patterning of compliant substrate and soft, conductive material networks. We demonstrate physically reconfigurable metamaterials that respond to mechanical stress in discrete modes leading to changes in the compliant conductor network to realize all digital logic functions and logic assemblies.

## Results

**A conductive mechanical metamaterial digital switch.** The metamaterials employ a constant cross-section consisting of a fundamental square tiling tessellation with square voids at the intersections. Shim et al.<sup>32</sup> report that this geometry exhibits a negative Poisson's ratio and a fully compacted state wherein the porosity of the compacted material is 0% in the ideal case of kinematic reconfiguration. In Fig. 1, we integrate this substrate architecture with conductive ink patterns that leverage the deformation of the metamaterial to reconfigure electrical circuits in discrete modes. Through this report, we build upon such fundamental building block to formulate all digital logic gates and to establish gate assembly and interconnection methods.

The elastomeric material substrates considered here are fabricated by casting liquid urethane rubber (Smooth-On VytaFlex 60) in 3D-printed molds (FlashForge Creator Pro) containing the negative of the sample architecture. The substrates also include surface channels in which the conductive networks are applied, Fig. 1(a). The conductive ink utilized in the channels is a composite containing silver (Ag) microflakes (Inframat Advanced Materials, 47MR-10F) and thermoplastic polyurethane (TPU) elastomer (BASF Elastollan Soft 35 A) to create conductive percolating networks. Copper wire leads that pass through the specimen via internal channels allow for electrical connections from an external voltage source or readout to the Ag-TPU trace terminals. Complete sample fabrication and characterization details are given in the Supplementary Information.

The metamaterials studied in this report are referred to by the unit cell that constructs the constant cross-section architecture. In Fig. 1(a), the metamaterial is assembled from  $C_2$  unit cells to be characterized more fully in the subsequent section of this report. An Ag-TPU trace pattern is applied to the elastomeric substrate.

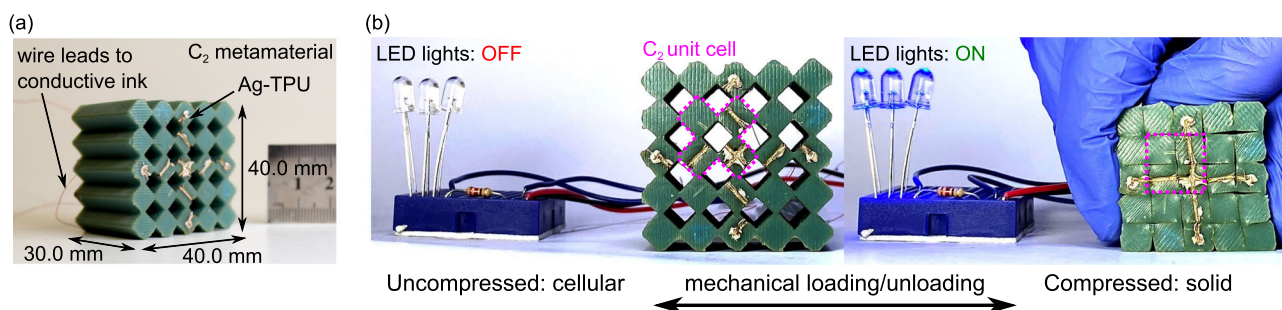


**Fig. 1** Compaction principle of electrical network switching in soft, conductive mechanical metamaterials. **a** Introduction of a metamaterial composed of  $C_2$  unit cell with conductive Ag-TPU trace. **b**  $C_2$  metamaterial in series with a power source and LED array to illustrate switching functionality. Uncompressed: Open circuit, LED off. Compacted: Closed circuit, LED on.

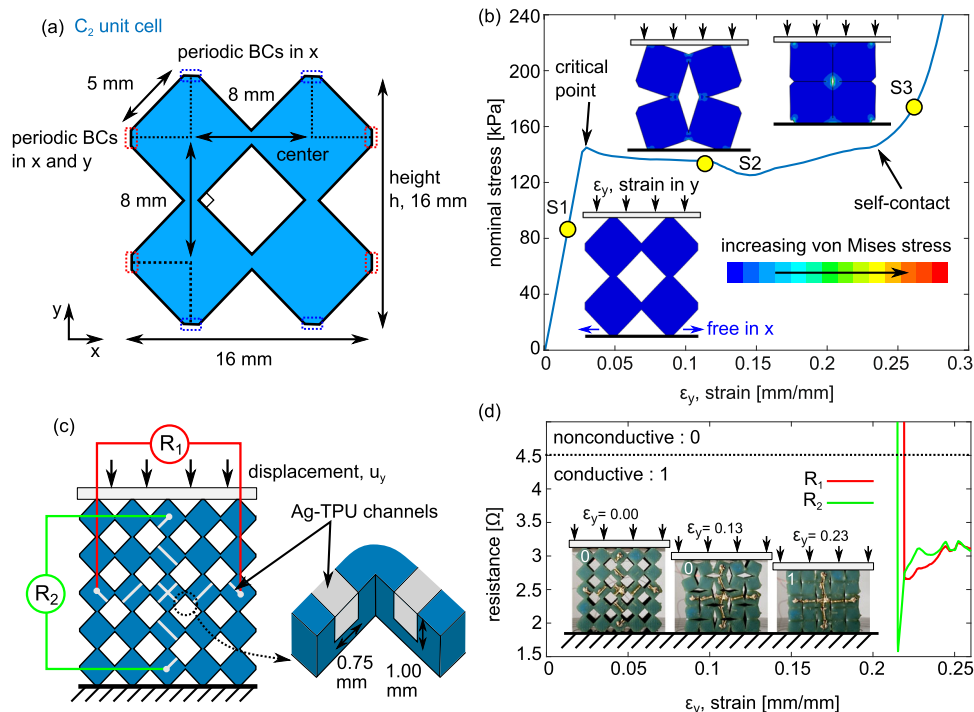


**Fig. 2 Bit abstraction via open/closed circuit. a** C<sub>2</sub> unit cell dimensions with periodic boundary conditions. **b** Simulated mechanical response of C<sub>2</sub> unit cell featuring three regimes of general behavior and shape change. **c** Schematic of C<sub>2</sub> metamaterial with Ag-TPU biaxial switch network. Resistance measurements R<sub>1</sub> and R<sub>2</sub> are monitored across two terminal pairs. **d** Experimental resistance measurement with photos depicting the deformations in the three compression regimes.

An electrical power supply and LED array are interfaced in series with the silver trace terminals at the sample leftmost and rightmost sides, respectively. By applying uniaxial displacement to the top of the metamaterial, the sample deforms into a fully compacted solid square Fig. 1(b). As a result, the Ag-TPU network closes through self-contact, passing electrical current through the LED array. Once the mechanical load is released, the Ag-TPU network opens and the LED array turns off again. Continued cycling of the metamaterial repeats the electrical switch behavior. The principle of reversible mechanical-electrical switching demonstrated in Fig. 1 is harnessed in this report to formulate all logic gate operations and logic assembly methods in a class of soft, conductive mechanical metamaterials.

To characterize the elastic buckling deformation of the metamaterial unit cells, we develop a finite element model that simulates the material response observed in experiments (see Supplementary Information). The C<sub>2</sub> unit cell geometry is shown in Fig. 2(a). The unit cell consists of two rows and two columns of a continuous square tiling pattern. A hyperelastic Neo-Hookean material model is employed on the 2D cross-section, considering plane strain assumptions and accounting for nonlinear deformations under quasi-static, uniaxial compressive displacement in the vertical direction  $u_y$ . Periodic boundary condition displacements in  $x$  and  $y$  are applied on the nodes highlighted with the dashed blue and red lines in Fig. 2(a).

The mechanical response for the C<sub>2</sub> unit cell illustrates three regimes during uniaxial compression, Fig. 2(b). Linear elastic response (label S1) occurs for small applied strains  $\epsilon_y = u_y/h$ , such as <2% strain. At a critical strain, namely  $\epsilon_{critical} = 0.0279$  in Fig. 2(b), a second regime (label S2) displays large decrease in uniaxial stiffness and a rotational behavior of the unit cell. With further increase in strain, a final transition occurs wherein self-contact and near-total compaction of the unit cell is achieved (label S3), leading to increase in uniaxial stiffness. For unit cell C<sub>2</sub>,

the self-contact strain is  $\epsilon_{contact} = 0.23$ . The compact state in Fig. 2 (b) represents the compacted shape of the experimental sample in Fig. 1(c) that closes the electrical circuit by self-contact of the Ag-TPU trace.

To demonstrate the relationship between the mechanical and electrical behavior by the compaction principle, we design a biaxially functional electrical switch Ag-TPU trace pattern on the surface of a metamaterial composed of C<sub>2</sub> unit cells, Fig. 2(c). The metamaterial is loaded quasi-statically in the vertical direction between rigid aluminum platens using a load frame (see Supplementary Information). Voltage divider circuits measure the electrical resistances R<sub>1</sub> and R<sub>2</sub> across the horizontal and vertical Ag-TPU terminal pairs, respectively.

Using the C<sub>2</sub> unit cell geometry and the Ag-TPU network on the sample, the metamaterial functions as a strain gated switch. For instance, Fig. 2(d) shows that the resistances R<sub>1</sub> and R<sub>2</sub> through the Ag-TPU trace pairs exhibit a nonconductive, infinite resistance that represents a 0 digital readout. Once the contact strain  $\epsilon_{contact} = 0.23$  is reached, the networks close as observed by the sudden drops in R<sub>1</sub> and R<sub>2</sub> to mean resistances near 3 Ω. The closed electrical connections therefore represent a 1 digital readout. A supporting kinematic model of the C<sub>2</sub> unit cell confirms self-contact is induced near applied strain of  $\epsilon_{contact} = 0.201$ , Supplementary Fig. 2(a) (see Supplementary Information). The similarity between the sudden changes in resistances R<sub>1</sub> and R<sub>2</sub> illustrates that the electrical connections may be achieved biaxially despite uniaxial mechanical input. These results introduce a technique to exploit transitions between uncompressed and compacted states of soft, conductive mechanical metamaterials to govern digital electrical signals.

**Method for digital logic in conductive mechanical metamaterials.** We leverage this foundation to create logic gates controlled by mechanical deformation. Metamaterials composed from C<sub>2</sub> unit

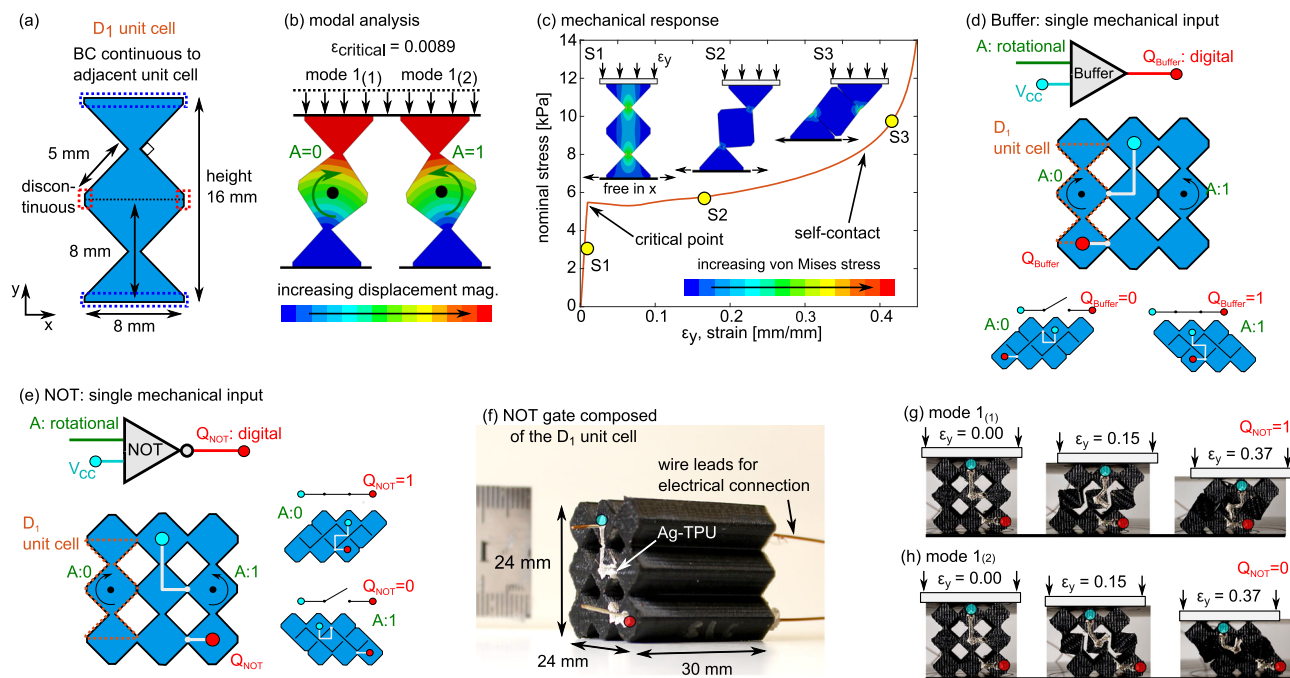


**Fig. 3** Bit abstraction via buckling direction. **a** D<sub>1</sub> unit cell dimensions with boundary conditions. **b** Modal analysis of D<sub>1</sub> unit cell with two deformation states, mode 1<sub>(1)</sub> and mode 1<sub>(2)</sub>. **c** Simulated mechanical response of D<sub>1</sub> unit cell featuring three deformation regimes. **d** Schematic of Buffer gate as direct electrical switch governed by a single mechanical rotation input, corresponding to the buckling mode. **e** Schematic and **(f)** experimental image of the NOT gate with one mechanical input rotation (green) and one digital output terminal (red) Q<sub>NOT</sub> on the metamaterial composed of D<sub>1</sub> unit cells. The powered input terminal is the cyan node, V<sub>cc</sub>. Photos of the NOT gate under uniaxial compression as it exhibits buckling **(g)** mode 1<sub>(1)</sub> and **(h)** mode 1<sub>(2)</sub>, along with the corresponding digital outputs Q<sub>NOT</sub> (red node).

cells may exhibit two rotations in the lowest order buckling mode, Supplementary Fig. 3. This limited switch behavior is a result of the distinct buckling modes and the choice of Ag-TPU network. As a result, we introduce a second unit cell termed D<sub>1</sub> that exploits a discontinuity with laterally adjacent unit cells in the left/right directions, Fig. 3(a).

A modal analysis of the D<sub>1</sub> unit cell is carried out to characterize the lowest order elastic buckling behavior. The unit cell top and bottom boundaries are relatively displaced with one side free to laterally displace in a given simulation. As shown in Fig. 3(b), the D<sub>1</sub> unit cell exhibits a buckling mode at a critical strain of 0.0089. Two states of deformation may occur for the same critical strain. Mode 1<sub>(1)</sub> exhibits a clockwise rotation of the central bulk material block, while mode 1<sub>(2)</sub> exhibits a counterclockwise rotation. Realization of these modes is dependent upon the vector of shear and uniaxial compression applied respecting the horizontal mirror plane. Uniaxial compression simulations are conducted to determine the mechanical properties of the D<sub>1</sub> unit cell. The results in Fig. 3(c) likewise reveal 3 collapse regimes similar in qualitative trend and interpretation with behavior of the C<sub>2</sub> unit cell in Fig. 2(b). The D<sub>1</sub> unit cell exhibits a lower critical strain  $\epsilon_{critical} = 0.0089$  and a greater self-contact strain  $\epsilon_{contact} = 0.40$  compared with the C<sub>2</sub> unit cell. A noticeable difference is also evident in the compacted states. Namely, the D<sub>1</sub> unit cell compacts into a parallelogram cross-section Fig. 3(c), compared with the square compacted state for the C<sub>2</sub> unit cell Fig. 2(b). Consequently, the metamaterial unit cells permit unique approaches to Ag-TPU trace networking to realize reconfigurable electrical interconnects.

Digital logic gates are provided with digital inputs and pass digital outputs. Our formulation of digital logic intrinsically couples discrete mechanical behavior with electrical signals passed through the metamaterials. Here, we consider a circuit powering node provided to an input terminal of the unit cell. The

input node is highlighted in cyan color and labeled as V<sub>cc</sub> on the NOT logic gate material shown in Fig. 3(d). The output node is highlighted in red color. To provide the digital logic operations, we exploit the mechanical buckling modes, considering counterclockwise rotation of the D<sub>1</sub> unit cell as a digital input of 1 and clockwise rotation as a digital input of 0, according to electrical conduction through the D<sub>1</sub> unit cell layer. The fundamental Buffer gate exemplifies this digitizing behavior as seen in Fig. 3(d), where counterclockwise rotational collapse of the D<sub>1</sub> unit cell metamaterial outputs Q<sub>Buffer</sub> of 1, and Q<sub>Buffer</sub> of 0 for clockwise rotation. The Buffer metamaterial gate is realized by three D<sub>1</sub> unit cells that are tiled together, keeping the discontinuity at the central bulk material block. The Ag-TPU trace applied to the surface realizes a switch that operates in agreement to Buffer logic in accordance with buckling modes of this metamaterial.

The NOT digital logic gate is an inverter of a digital signal, converting a 0 to a 1, and vice versa. The NOT gate is thus an inverted Buffer gate. In this embodiment of soft digital logic, output signal inversion is achieved by a horizontal or vertical mirroring of the conductive network. The metamaterial realization of the NOT logic gate that we explore here is shown in Fig. 3 (e) along with the corresponding logic outputs resulting from each of the clockwise and counterclockwise collapse rotations. The output digital signal Q<sub>NOT</sub> is 1 for the conductive Ag-TPU network in Fig. 3(g) considering the clockwise rotation of the central bulk material blocks in the unit cells. Conversely, an output digital signal Q<sub>NOT</sub> of 0 is read out for the buckling mode with counterclockwise bulk material block rotation, Fig. 3(h). As expected, these results are the opposite of the Buffer gate fundamental switch. Consequently, the digital logic realized by the discrete, modal mechanical deformation of the metamaterial in Fig. 3(f) is analogous to a digital NOT gate. Moreover, Fig. 3 (g), (h) show that the collapse behavior and thus digital signaling

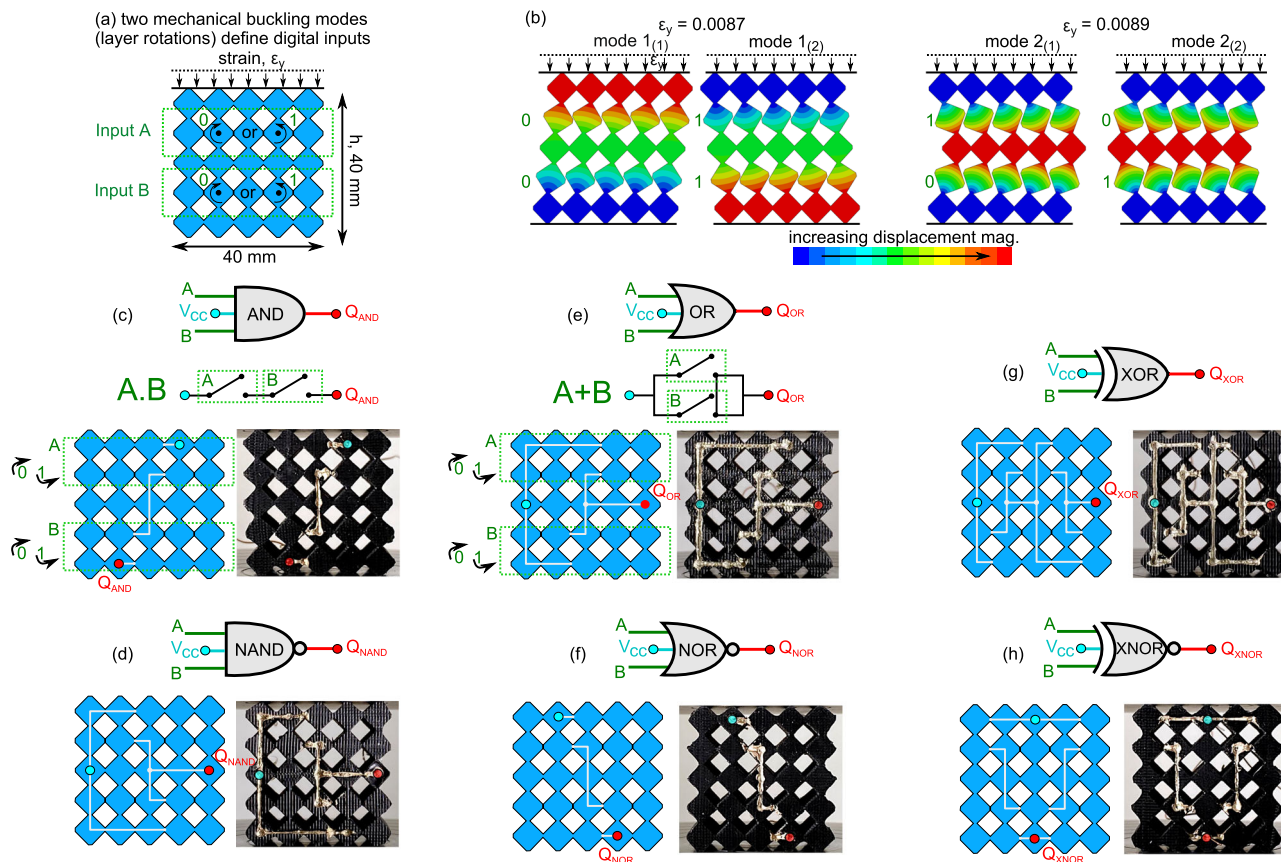


**Fig. 4 Formulation of digital logic gates in soft, conductive mechanical metamaterials.** **a** Schematic of the  $D_1$  based metamaterials. Inputs A and B are the rotations in the first and second layers, respectively. **b** Modal analysis illustrating four possible deformation states. Schematics and experimental images of the Ag-TPU network on the metamaterials for **(c)** AND, **(d)** NAND, **(e)** OR, **(f)** NOR, **(g)** XOR, and **(h)** XNOR logic gates. AND and OR include corresponding switched circuit schematics. Each gate contains two mechanical inputs A and B (green) and one digital output Q (red). The powered input terminal is the cyan node,  $V_{cc}$ .

occurs for the same values of applied strain. This indicates that exploitation of small perturbations around the bifurcation<sup>33</sup>, or critical strain, could be used for high sensitivity control<sup>34</sup> of the combined mechanical and electrical functions of the soft, conductive logic gate.

**Formulation of all digital logic gates.** We build on this manifestation of soft, conductive matter-based digital logic to realize the remaining 6 logic gates: AND, NAND, OR, NOR, XOR, and XNOR. We use two rows of  $D_1$  unit cells each containing 5 unit cells to realize the metamaterial geometries shown in Fig. 4(a). The unit cells share the central row of bulk material blocks, which does not influence the layer-by-layer mechanics. We undertake a modal analysis of the materials to identify low order buckling modes. Two modes are found for critical strains 0.0087 and 0.0089, while each mode may be manifest in two deformation states, Fig. 4(b). These modes are realized by the specific vector combination of shear and uniaxial stresses applied to the top metamaterial surface. For instance, mode  $1_{(1)}$  requires shear to the right and then uniaxial compression, while mode  $2_{(1)}$  requires uniaxial compression then shear to the left near the critical strain, and vice versa for the mode  $1_{(2)}$  and mode  $2_{(2)}$ . Thus, the logic inputs are represented by the layer-by-layer rotations, illustrated in Fig. 4(a) with green labels. Input A of the soft, conductive logic gate indicates the rotation of the top layer of unit cells, while Input B indicates the rotation of the bottom layer of unit cells. This introduces a unique technique to control mechanical digital

inputs through stress vectors and discrete self-contact states in soft mechanical metamaterials<sup>35</sup>.

The Ag-TPU trace networks required to realize the AND, NAND, OR, NOR, XOR, and XNOR gates in this formulation of soft digital logic are shown in Fig. 4(c)–(h). By using the fundamental Buffer or NOT logic gate Fig. 3(d) for each mechanical input layer and by electrically networking the outputs of each layer in series or parallel, the remaining AND, NAND, OR, NOR, XOR, and XNOR logic gates may be realized in a systematic way. For the AND and OR gates, the corresponding serial and parallel circuit schematics are shown in Fig. 4(c), (e). The relations between the serial (AND) and parallel (OR) switch assembly schematics and conductive trace networks are apparent considering Fig. 4(c), (e). Based on the induced mode in Fig. 4(b), the switches open or close according to (counter) clockwise assignment of (1)0 digital bits via the Ag-TPU trace networks to result in the appropriate digital output, Q. For instance, the AND gate registers  $Q_{AND} = 1$  when both layers rotate counterclockwise, or 1. Thus, a clear analogy exists between the circuitry schematic, the Ag-TPU network topology, and the mechanical buckling deformations. The Ag-TPU trace networks shown in Fig. 4 are not unique and can be tailored to permit changing positions of the powered node (highlighted in cyan color) and output node (red color). The reading from the output nodes (red color) represent the digital output from the soft, conductive logic gate.

Gates such as the NAND in Fig. 4(d) and OR in Fig. 4(e) contain the same fundamental parallel circuit design, yet are

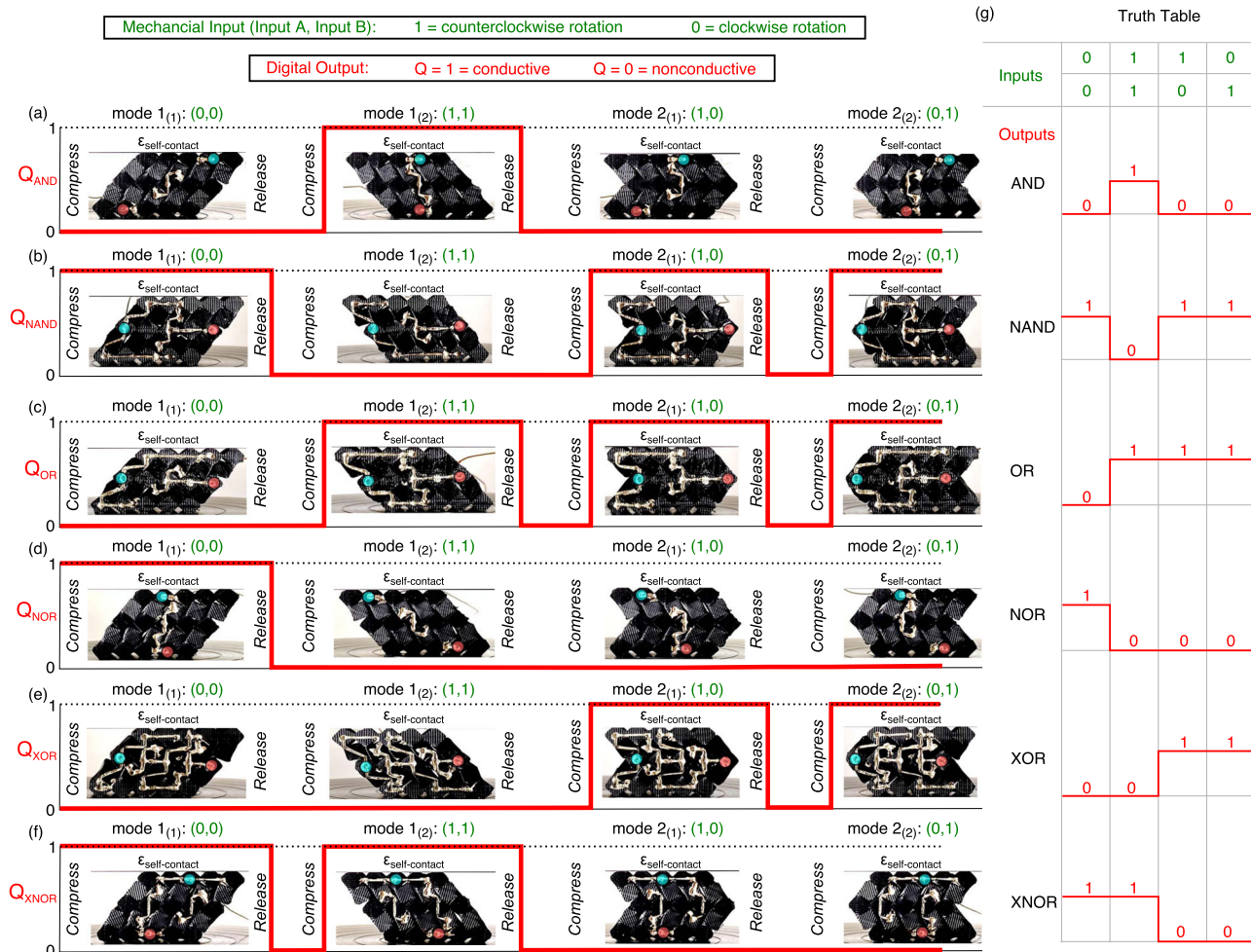


**Fig. 5 Processing all digital logic operations in soft, conductive mechanical metamaterials.** Logic gate digital output Boolean response at each of the four compact states for the (a) AND, (b) NAND, (c) OR, (d) NOR, (e) XOR, and (f) XNOR logic gate. The respective mechanical inputs (green) for each of the deformation states directly relate to (g) the logic gates truth table inputs.

vertically mirrored according to the horizontal midplane. The NAND network topology is obtained by applying De Morgan's theorem, which states that the NAND gate is equivalent to an inverted OR gate. As described above related the NOT to the Buffer, the inversion operation in this embodiment of soft digital logic gates is a vertical or horizontal mirroring of the conductive trace network. As a result, De Morgan's theorem is readily applied to create the NAND metamaterial gate Fig. 4(d) via the base construct of the OR metamaterial gate Fig. 4(e). DeMorgan's theorem is also applied to design the NOR gate Fig. 4(f) from the embodiment of the AND gate Fig. 4(c). Finally, the XOR metamaterial gate Fig. 4(g) and XNOR gate Fig. 4(h) are obtained through a serial combination of OR-NAND gates and parallel combination of AND-NOR gates, respectively. Such design protocol is directly analogous to the formulation of conventional switched electrical networks that provide digital logic functionality.

To validate the functioning of the logic gates, samples are fabricated and compressed using the experimental setup in Supplementary Fig. 1(b). Each of the buckling modes is achieved through cyclic loading and unloading. Figure 5 compiles photographs of deformed modes, resulting Ag-TPU network connectivity, and associated truth tables.

The experimental digital outputs for each buckling mode behavior agree with the respective truth table entry for the ideal logic gates, Fig. 5. For instance, the AND gate in Fig. 5(a) provides

a digital output  $Q_{AND} = 1$  for mode  $1_{(2)}$  when both mechanical inputs are counterclockwise rotations, and a digital output of  $Q_{AND} = 0$  for all other combinations. The Supplementary Video 1 shows the transitions among the digitized, modal inputs, and the digital outputs, with an LED array indicator for visualization.

## Discussion

This foundation is extensible to the formulation of logic gate combinations used in integrated circuits. For instance, Supplementary Fig. 9 demonstrates a three-input logic gate combination of OR-NAND on a three layer metamaterial. To create the OR-NAND network topology, a negated OR gate Fig. 4(e) interfaces with the NAND gate parallel switch Fig. 4(d). Interestingly, by the unique  $D_1$  unit cell design explored here, metamaterial gates with  $n$  layers possess  $2^n$  self-contacting buckling modes, in agreement with the number of binary input combinations for the  $n$  input gate assembly. This differentiating characteristic allows for a systematic metamaterial design process to generate arbitrary gate combinations via strategic conductive trace network topologies (see Supplementary Information), although the platforms are not as much assembled from modules as they are designed into a monolithic metamaterial circuit. Explorations of modularly assembled soft logic gates using our mechanical metamaterial modules may take inspiration from mechanical signal transmission concepts<sup>26,27</sup> as well as techniques explored

with pneumatic-mechanical realizations of soft logic<sup>30</sup>. Although the logic gates formulated here do not compete with the speed and component scaling of conventional digital microprocessors, the conductive metamaterial-based information processing may provide essential robustness of function and material compatibility for future autonomous soft matter that emulate numerous biological systems.

By establishing interfaces between soft mechanical metamaterials and digital logic gating, this work formulates a general method to synthesize discrete mechanical configurations with conductive networks to govern digital electrical outputs. As one manifestation of soft, smart matter<sup>36</sup>, the mechanical metamaterial building blocks exploited in this work may be considered as building blocks for future soft matter assemblies, such as to realize autonomous soft machines with integrated sensory, actuation, and decision-making functionalities<sup>37</sup>. The concepts embodied in this report are also free of length-scale dependence, by leveraging nominally kinematic rearrangement of cellular solids<sup>32</sup>, and suggest one means to process mechanical stress inputs without need for periodic sensor observation. Consequently, physical embodiments of these principles may be exploited for low-power information processing in fields as diverse as DNA origami<sup>38</sup>, electro-optical filters<sup>39</sup>, reconfigurable antenna<sup>40</sup>, and more.

## Methods

### Specimen fabrication methods

**Metamaterial substrate fabrication.** The elastomeric metamaterial substrates are fabricated by casting liquid urethane rubber (Smooth-On VytaFlex 60) in a two-part mold. The mold parts are designed in CAD software SOLIDWORKS and 3D-printed (FlashForge Creator Pro) with acrylonitrile butadiene styrene (ABS) filament. When assembled together, the two-part mold realizes the negative of the metamaterial substrate shape. The liquid urethane rubber utilized in this research is a two-part material, A and B parts that are initially mixed in a 1 A:1 B volume ratio and stirred by hand for 2 min. After the material is poured into the mold, it is cured for 24 h. The sample is then carefully demolded and prepared for testing. Metamaterials using  $C_2$  and  $D_1$  unit cells are prepared utilizing this procedure.

**Conductive ink fabrication and deposition.** The conductive ink utilized in the channels is a composite containing 35% (volume %, v%) silver (Ag) microflakes (Inframat Advanced Materials, 47MR-10F) and 65% (v%) thermoplastic polyurethane (TPU) elastomer (BASF Elastollan Soft 35 A). To begin processing the conductive ink, Ag microflakes are first mixed in a glass vial with sufficient N-Methyl-2-pyrrolidone (NMP) solvent, and sonicated (Branson M2800 Ultrasonic Cleaner) for 60 min. TPU is then added to the Ag-NMP mixture, and planetary mixed (KK 300SS Mazerustar) at 225 × g for 2-minute increments. The planetary mixing process is repeated three times with gentle hand stirring in between to ensure walls of the vial do not collect excess Ag or TPU particles. After the mixture is given 48 h for the NMP to evaporate at room temperature, the Ag-TPU ink is ready for application.

Enamel-coated copper wire (22 gauge) leads are passed through small molded-in 1.50 mm diameter channels in the substrate to terminate at the front cross-sections of the metamaterials. Metamaterial photographs in Figs. 1 and 3 of the main text and in the Supplementary Video 1 show more clearly how the copper wires terminate at the front cross-sections. Enamel is only removed from both extremities of the copper wire ends to eliminate trace electrical shorting along the wire length. To secure the wire leads in the channels through the substrates, a small amount of silicone adhesive (DAP All-Purpose) is deposited by syringe in the internal channels through the rear-facing cross-section. Using a 3.0 cc dispensing syringe, the surface channels on the substrate are filled with Ag-TPU ink and allowed to cure around the copper wire leads for 24 h.

**Experimental characterization methods.** The unit cells  $C_2$  and  $D_1$  and metamaterials assembled from the unit cells are examined using distinct experimental methods by virtue of the unique mechanical behaviors that motivate distinct electrical circuit switching methods. The specimens are quasi-statically and vertically displaced  $u_y$  by a polished, rigid platen from a load frame (ADMET eXpert 5600) at a loading rate of 0.5 mm min<sup>-1</sup>, shown in Supplementary Fig. 1. A laser displacement sensor (Micro-Epsilon optoNCDT ILD1700-200) is attached to the load frame to measure vertical displacements  $u_y$  of the platen. For metamaterial  $C_2$ , the bottom specimen surface rests on a polished, fixed aluminum plate, Supplementary Fig. 1(a). As a result, for  $C_2$  the top and bottom surfaces of the specimen have limited motion in lateral displacements  $u_x$  due to friction against the platen

and plate. The uniaxial applied strain is calculated from  $\epsilon_y = u_y/h$  where  $h$  is the macroscopic height of the metamaterial sample or unit cell.

For metamaterial  $D_1$ , the bottom surface is presumed to slide in the simulations reported in the main text. To permit lateral sliding of metamaterials in the experimental characterization, we place a polished, rigid aluminum plate on smooth cylindrical shafts that act as a rolling surface for the bottom of the  $D_1$  samples, Supplementary Fig. 1(b). Such a setup provides uninhibited lateral displacements  $u_x$ . The direction of cross-section rotation in experiments may be governed at critical points by manual methods in order to achieve all buckling modes, since only the lowest order mode occurs naturally in the absence of additional control measures. Voltage divider circuits are used to measure resistance through the Ag-TPU ink traces with a 1.30 Ohm reference resistor, where the electrical resistances  $R_1$  and  $R_2$  are evaluated across the horizontal and vertical Ag-TPU terminal pairs, respectively. Data is collected through an acquisition system (NI USB 6341 Multifunction DAQ) and analyzed in MATLAB.

**Finite element modeling methods.** ABAQUS Linear Buckling Perturbation and Dynamic-Implicit simulations are conducted with 2D plane strain models based on the constant material cross section. For the Linear Buckling Perturbation simulations, a subspace eigensolver is used to determine the low-order buckling modes. For the nonlinear Dynamic-Implicit step, a time period that is proportional to the 0.5 mm.min<sup>-1</sup> quasi-static experimental load frame loading rate is used. A hyperelastic Neo-Hookean material model is employed with Young's modulus of 2.07 MPa and Poisson's ratio of 0.499 for the samples considered here. Free quadrilateral elements are used for all geometry meshes with seed sizes proportional to the smallest geometric feature with at least 0.25 ratio of element characteristic dimension to substrate feature size.

For the  $C_2$  unit cell, periodic boundary conditions are imposed on the outermost nodes while the bottom boundaries are fixed in  $y$  and free to slide in  $x$ . Shown in Fig. 2(a) in the main text, the left-most and right-most boundary nodes (outlined in red) are constrained to mirror the displacements of nodes in  $x$  and  $y$ , and similarly the top-most and bottom-most boundary nodes (outlined in blue) are constrained to mirror displacements only in  $x$ . For the  $D_1$  unit cell and metamaterial assemblies the boundaries are fixed in  $y$  and free to slide in  $x$  at the bottom edge.

By applying compressive displacements  $u_y$  at the top boundary of the unit cells and metamaterial assemblies, we acquire the buckling modes as well as the mechanical properties through the Linear Perturbation and Dynamic-Implicit simulations, respectively.

**Statistics and reproducibility.** All experiments and simulations are conducted a minimum of 6 times to confirm repeatability of trends and quantities.

### Data availability

Models, codes, and datasets generated during and/or analyzed during the current study are available from the corresponding author on request. All data is available in the main text or the Supplementary Information.

Received: 7 August 2020; Accepted: 4 February 2021;

Published online: 12 March 2021

## References

- Harris, K. D., Elias, A. L. & Chung, H.-J. Flexible electronics under strain: a review of mechanical characterization and durability enhancement strategies. *J. Mater. Sci.* **51**, 2771–2805 (2016).
- Rogers, J. A., Someya, T. & Huang, Y. Materials and mechanics for stretchable electronics. *Science* **327**, 1603–1607 (2010).
- Zhu, J., Dexheimer, M. & Cheng, H. Reconfigurable systems for multifunctional electronics. *npj Flex. Electron.* **1**, 206–214 (2017).
- Nassar, J. M., Rojas, J. P., Hussain, A. M. & Hussain, M. M. From stretchable to reconfigurable inorganic electronics. *Extrem. Mech. Lett.* **9**, 245–268 (2016).
- Huang, S., Liu, Y., Zhao, Y., Ren, Z. & Guo, C. F. Flexible electronics: stretchable electrodes and their future. *Adv. Funct. Mater.* **29**, 1805924 (2019).
- Palleau, E., Reece, S., Desai, S. C., Smith, M. E. & Dickey, M. D. Self-healing stretchable wires for reconfigurable circuit wiring and 3D microfluidics. *Adv. Mater.* **25**, 1589–1592 (2013).
- Ilyas, N., Cook, A. & Tabor, C. E. Designing liquid metal interfaces to enable next generation flexible and reconfigurable electronics. *Adv. Mater. Interfaces* **4**, 1700141 (2017).
- Markvicka, E. J., Barlett, M. D., Huang, X. & Majidi, C. An autonomously electrically self-healing liquid metal-elastomer composite for robust soft-matter robotics and electronics. *Nat. Mater.* **17**, 618–624 (2018).
- Valentine, A. D. et al. Hybrid 3D printing of soft electronics. *Adv. Mater.* **29**, 1703817 (2017).

10. Sears, N. C., Berrigan, J. D., Buskohl, P. R. & Harne, R. L. Flexible hybrid electronic material systems with programmable strain sensing architectures. *Adv. Funct. Mater.* **20**, 1800499 (2018).
11. Merilampi, S., Laine-Ma, T. & Ruuskanen, P. The characterization of electrically conductive silver ink patterns on flexible substrates. *Microelectron. Reliab.* **49**, 782–790 (2009).
12. Sears, N. C., Berrigan, J. D., Buskohl, P. R. & Harne, R. L. Dynamic response of flexible hybrid electronic material systems. *Composite Struct.* **208**, 377–384 (2019).
13. Zhang, Y. et al. A mechanically driven form of Kirigami as a route to 3D mesostructures in micro/nanomembranes. *Proc. Natl Acad. Sci.* **112**, 11757–11764 (2015).
14. Rogers, J., Huang, Y., Schmidt, O. G. & Gracias, D. H. Origami mems and nems. *MRS Bull.* **41**, 123–129 (2016).
15. Xu, B., Chen, D. & Hayward, R. C. Mechanically gated electrical switches by creasing of patterned metal/elastomer bilayer films. *Adv. Mater.* **26**, 4381–4385 (2014).
16. Nick, Z. H., Tabor, C. E. & Harne, R. L. Liquid metal microchannels as digital sensors in mechanical metamaterials. *Extrem. Mech. Lett.* **40**, 100871 (2020).
17. Heo, H., Li, S., Bao, H. & Ju, J. A passive thermal switch with kirigami-inspired mesostructures. *Adv. Eng. Mater.* **21**, 1900225 (2019).
18. Xie, K. et al. Brain computation is organized via power-of-two-based permutation logic. *Front. Syst. Neurosci.* **10**, 95 (2016).
19. Bilal, O. R., Foehr, A. & Daraio, C. Bistable metamaterial for switching and cascading elastic vibrations. *Proc. Natl Acad. Sci.* **114**, 4603–4606 (2017).
20. Dhasarathan, V., Sahu, S. K., Nguyen, T. K. & Palai, G. Realization of all logic gates using metamaterials based three dimensional photonics structures: a future application of 3D photonics to optical computing. *Opt. - Int. J. Light Electron Opt.* **202**, 163723 (2020).
21. Jin, Y. et al. Materials tactile logic via innervated soft thermochromic elastomers. *Nat. Commun.* **10**, 4187 (2019).
22. Reif, J. H., *Computational Complexity: Theory, Techniques, and Applications* (Springer, New York, 2012), pp. 1821–1836.
23. Merkle, R. C. Two types of mechanical reversible logic. *Nanotechnology* **4**, 114–131 (1993).
24. Harne, R. L. & Wang, K. W., *Harnessing Bistable Structural Dynamics: for Vibration Control, Energy Harvesting and Sensing* (John Wiley & Sons Ltd., Chichester, 2017).
25. Kochmann, D. M. & Bertoldi, K. Exploiting microstructural instabilities in solids and structures: from metamaterials to structural transitions. *Applied Mechanics Reviews*, 050801 (2017).
26. Song, Y. et al. Additively manufacturable micro-mechanical logic gate. *Nat. Commun.* **10**, 1–6 (2019).
27. Ion, A., Wall, L., Kovacs, R. & Baudisch, P. *Digital Mechanical Metamaterials*, presented at Proceedings of the 2017 CHI Conference on Human Factors in Computing Systems (New York, 2017).
28. Jiang, Y., Korpas, L. M. & Raney, J. R. Bifurcation-based embodied logic and autonomous actuation. *Nat. Commun.* **10**, 128 (2019).
29. Treml, B., Gillman, A., Buskohl, P. & Vaia, R. Origami mechanologic. *Proc. Natl Acad. Sci.* **115**, 6916–6921 (2018).
30. Preston, D. J. et al. Digital logic for soft devices. *Proc. Natl Acad. Sci.* **116**, 7750–7759 (2019).
31. Tortora, G. J. & Derrickson, B. H. *Principles of Anatomy and Physiology* (John Wiley and Sons, Inc., New York, 2006).
32. Shim, J. et al. Harnessing instabilities for design of soft reconfigurable auxetic/chiral materials. *Soft Matter* **9**, 8198–8202 (2013).
33. Scheffer, M. et al. Anticipating critical transitions. *Science* **338**, 344–348 (2012).
34. McInnes, C. R. & Waters, T. J. Reconfiguring smart structures using phase space connections. *Smart Mater. Struct.* **17**, 025030 (2008).
35. El-Helou, C. & Harne, R. L. Exploiting functionally graded elastomeric materials to program collapse and mechanical properties. *Adv. Eng. Mater.* **21**, 1900807 (2019).
36. Pishvar, A. & Harne, R. L. Foundations for soft, smart matter by active mechanical metamaterials. *Adv. Sci.* **7**, 2001384 (2020).
37. Majidi, C. Soft-matter engineering for soft robotics. *Adv. Mater. Technol.* **4**, 1800477 (2019).
38. Marras, A. E., Zhou, L., Su, H. J. & Castro, C. E. Programmable motion of DNA origami mechanisms. *Proc. Natl Acad. Sci.* **112**, 713–718 (2015).
39. Zhang, Y. et al. One-step nanoscale assembly of complex structures via harnessing of an elastic instability. *Nano Lett.* **8**, 1192–1196 (2008).
40. Kim, H. et al. Responsive, 3D electronics enabled by liquid crystal elastomer substrates. *ACS Appl. Mater. Interfaces* **11**, 19506–19513 (2019).

### Acknowledgements

**Funding:** This research is supported in part by a U.S. Air Force Research Lab (AFRL) Summer Faculty Fellowship and in part by the National Science Foundation (NSF) Faculty Early Career Development Award (No. 2054970).

### Author contributions

C.E.H. and R.L.H. designed the research; C.E.H. performed research; C.E.H., P.R.B., C.E.T., and R.L.H. analyzed the data; and C.E.H., P.R.B., C.E.T., and R.L.H. wrote the paper.

### Competing interests

The authors declare no competing interests.

### Additional information

**Supplementary information** The online version contains supplementary material available at <https://doi.org/10.1038/s41467-021-21920-y>.

**Correspondence** and requests for materials should be addressed to R.L.H.

**Peer review information** *Nature Communications* thanks Andrew Pascall and the other, anonymous, reviewer(s) for their contribution to the peer review of this work. Peer reviewer reports are available.

**Reprints and permission information** is available at <http://www.nature.com/reprints>

**Publisher's note** Springer Nature remains neutral with regard to jurisdictional claims in published maps and institutional affiliations.



**Open Access** This article is licensed under a Creative Commons Attribution 4.0 International License, which permits use, sharing, adaptation, distribution and reproduction in any medium or format, as long as you give appropriate credit to the original author(s) and the source, provide a link to the Creative Commons license, and indicate if changes were made. The images or other third party material in this article are included in the article's Creative Commons license, unless indicated otherwise in a credit line to the material. If material is not included in the article's Creative Commons license and your intended use is not permitted by statutory regulation or exceeds the permitted use, you will need to obtain permission directly from the copyright holder. To view a copy of this license, visit <http://creativecommons.org/licenses/by/4.0/>.

© The Author(s) 2021



# Supplementary Information for Digital Logic Gates in Soft, Conductive Mechanical Metamaterials

Charles El Helou, Philip R. Buskohl, Christopher E. Tabor, and Ryan L. Harne

Correspondence to: ryanharne@psu.edu

## 1 Methods

### 1. Specimen fabrication methods

#### *1.1 Metamaterial substrate fabrication*

The elastomeric metamaterial substrates are fabricated by casting liquid urethane rubber (Smooth-On VytaFlex 60) in a two-part mold. The mold parts are designed in CAD software SOLIDWORKS and 3D-printed (FlashForge Creator Pro) with acrylonitrile butadiene styrene (ABS) filament. When assembled together, the two-part mold realizes the negative of the metamaterial substrate shape. The liquid urethane rubber utilized in this research is a two-part material, A and B parts that are initially mixed in a 1A:1B volume ratio and stirred by hand for 2 minutes. After the material is poured into the mold, it is cured for 24 hours. The sample is then carefully demolded and prepared for testing. Metamaterials using C2 and D1 unit cells are prepared utilizing this procedure.

#### *1.2 Conductive ink fabrication and deposition*

The conductive ink utilized in the channels is a composite containing 35% (volume %, v%) silver (Ag) microflakes (Inframat Advanced Materials, 47MR-10F) and 65% (v%) thermoplastic polyurethane (TPU) elastomer (BASF Elastollan Soft 35A). To begin processing the conductive ink, Ag microflakes are first mixed in a glass vial with sufficient N-Methyl-2-pyrrolidone (NMP) solvent, and sonicated (Branson M2800 Ultrasonic Cleaner) for 60 minutes. TPU is then added to

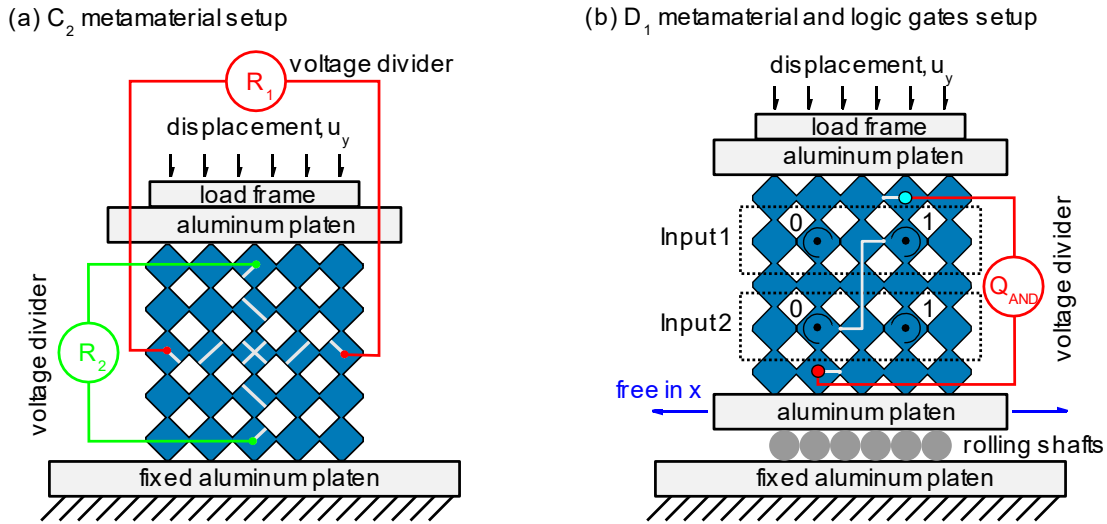
the Ag-NMP mixture, and planetary mixed (KK 300SS Mazerustar) at  $225 \times g$  for 2-minute increments. The planetary mixing process is repeated 3 times with gentle hand stirring in between to ensure walls of the vial do not collect excess Ag or TPU particles. After the mixture is given 48 hours for the NMP to evaporate at room temperature, the Ag-TPU ink is ready for application.

Enamel-coated copper wire (22 gauge) leads are passed through small molded-in 1.50 mm diameter channels in the substrate to terminate at the front cross-sections of the metamaterials. Metamaterial photographs in Figures 1 and 3 of the main text and in the Supplementary Video 1 show more clearly how the copper wires terminate at the front cross-sections. Enamel is only removed from both extremities of the copper wire ends to eliminate trace electrical shorting along the wire length. To secure the wire leads in the channels through the substrates, a small amount of silicone adhesive (DAP All-Purpose) is deposited by syringe in the internal channels through the rear-facing cross-section. Using a 3.0 cc dispensing syringe, the surface channels on the substrate are filled with Ag-TPU ink and allowed to cure around the copper wire leads for 24 hours.

## **2. Experimental characterization methods**

The unit cells  $C_2$  and  $D_1$  and metamaterials assembled from the unit cells are examined using distinct experimental methods by virtue of the unique mechanical behaviors that motivate distinct electrical circuit switching methods. The specimens are quasi-statically and vertically displaced  $u_y$  by a polished, rigid platen from a load frame (ADMET eXpert 5600) at a loading rate of  $0.5 \text{ mm min}^{-1}$ , shown in Supplementary Figure 1. A laser displacement sensor (Micro-Epsilon optoNCDT ILD1700-200) is attached to the load frame to measure vertical displacements  $u_y$  of the platen. For metamaterial  $C_2$ , the bottom specimen surface rests on a polished, fixed aluminum

plate, Supplementary Figure 1(a). As a result, for  $C_2$  the top and bottom surfaces of the specimen have limited motion in lateral displacements  $u_x$  due to friction against the platen and plate. The uniaxial applied strain is calculated from  $\varepsilon_y = u_y / h$  where  $h$  is the macroscopic height of the metamaterial sample or unit cell.



**Supplementary Figure 1. Schematic of the experimental loading setup utilized for metamaterials composed of (a)  $C_2$  and (b)  $D_1$  unit cells. The AND gate circuitry is depicted in the schematic, yet such setup is used for all logic gates.**

For metamaterial  $D_1$ , the bottom surface is presumed to slide in the simulations reported in the main text. To permit lateral sliding of metamaterials in the experimental characterization, we place a polished, rigid aluminum plate on smooth cylindrical shafts that act as a rolling surface for the bottom of the  $D_1$  samples, Supplementary Figure 1(b). Such a setup provides uninhibited lateral displacements  $u_x$ . The direction of cross-section rotation in experiments may be governed at critical points by manual methods in order to achieve all buckling modes, since only the lowest

order mode occurs naturally in the absence of additional control measures. Voltage divider circuits are used to measure resistance through the Ag-TPU ink traces with a 1.30 Ohm reference resistor, where the electrical resistances  $R_1$  and  $R_2$  are evaluated across the horizontal and vertical Ag-TPU terminal pairs, respectively. Data is collected through an acquisition system (NI USB 6341 Multifunction DAQ) and analyzed in MATLAB.

### **3. Finite element modeling methods**

ABAQUS Linear Buckling Perturbation and Dynamic-Implicit simulations are conducted with 2D plane strain models based on the constant material cross section. For the Linear Buckling Perturbation simulations, a subspace eigensolver is used to determine the low-order buckling modes. For the nonlinear Dynamic-Implicit step, a time period that is proportional to the  $0.5 \text{ mm}\cdot\text{min}^{-1}$  quasi-static experimental load frame loading rate is used. A hyperelastic Neo-Hookean material model is employed with Young's modulus of 2.07 MPa and Poisson's ratio of 0.499 for the samples considered here. Free quadrilateral elements are used for all geometry meshes with seed sizes proportional to the smallest geometric feature with at least 0.25 ratio of element characteristic dimension to substrate feature size.

For the  $C_2$  unit cell, periodic boundary conditions are imposed on the outermost nodes while the bottom boundaries are fixed in  $y$  and free to slide in  $x$ . Shown in Figure 2(a) in the main text, the left-most and right-most boundary nodes (outlined in red) are constrained to mirror the displacements of nodes in  $x$  and  $y$ , and similarly the top-most and bottom-most boundary nodes (outlined in blue) are constrained to mirror displacements only in  $x$ . For the  $D_1$  unit cell and metamaterial assemblies the boundaries are fixed in  $y$  and free to slide in  $x$  at the bottom edge.

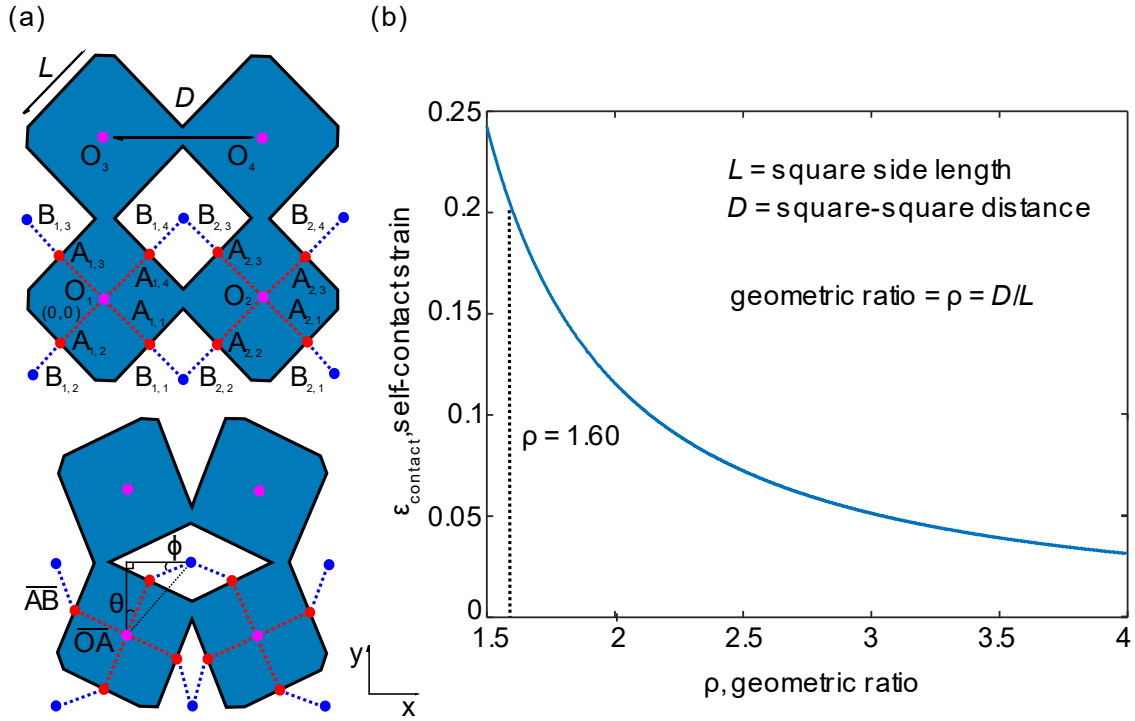
By applying compressive displacements  $u_y$  at the top boundary of the unit cells and metamaterial assemblies, we acquire the buckling modes as well as the mechanical properties through the Linear Perturbation and Dynamic-Implicit simulations, respectively.

#### **4. C<sub>2</sub> unit cell analysis**

This section includes supporting analysis conducted on the C<sub>2</sub> metamaterial unit cell including kinematic modeling and modal analysis.

##### *4.1 Kinematic model*

To understand the deformation of structures comprised from the continuous C<sub>2</sub> unit cell, we develop a kinematic model to characterize the rotation of unit cell constituents observed experimentally and computationally. The model is particularly utilized to predict the strain  $\varepsilon_y$  at self-contact  $\varepsilon_{contact}$ , at which electrical connection is presumed to occur. The geometry seen in Supplementary Figure 2(a) is used to model the system. The C<sub>2</sub> unit cell is comprised of four tessellated material blocks labeled at the respective block centers by coordinates  $O_n$  for the  $n^{th}$  block. Each block includes four coordinates at the center of the material sides labeled as  $A_{n,m}$  for the  $m^{th}$  side of the  $n^{th}$  block, and four coordinates at the center of the square voids adjacent to each side labeled as  $B_{n,m}$ .



**Supplementary Figure 2. (a) Schematics employed to derive the kinematic model for the  $C_2$  unit cell rotation. (b) Relationship between the geometric ratio and the self-contact strain.**

We assume that the material preserves shape of the solid bulk material blocks, so that the lengths  $|\overline{OA}|$  and  $|\overline{AB}|$  remain constant throughout the full rotation from uncompressed to compacted. The Equations (1) and (2) define  $|\overline{OA}|$  and  $|\overline{AB}|$ , respectively. The parameters  $D$  and  $L$  are identified as unit cell dimensions in Supplementary Figure 2(a).

$$|\overline{OA}| = \frac{\sqrt{2D} - L}{2} \quad (1)$$

$$|\overline{AB}| = \frac{L}{2} \quad (2)$$

Since the  $C_2$  unit cell has a single degree of freedom, we use the rotation angle  $\theta$  as the state variable. The angle  $\phi$  is then defined in terms of the state variable, as shown in Equation (3), assuming that the voids are regular squares.

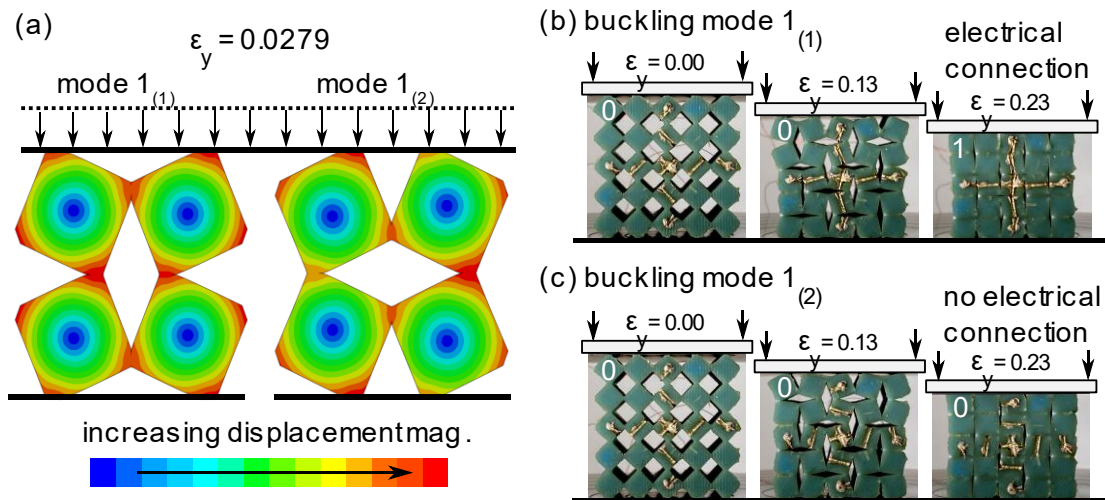
$$\phi = \frac{\pi}{4} - \sin^{-1}\left(\frac{2|\overline{OA}|}{L}\sin\left(\frac{\pi}{4} - \theta\right)\right) \quad (3)$$

We utilize Equations (1), (2), and (3) to determine the vectors  $\overline{OA}$  and  $\overline{AB}$  for a specific value of  $\theta$  induced by applied disturbances, such as the applied displacements in the computational and experimental characterization, Sec. 1. When adjacent solid material blocks of the  $C_2$  unit cell contact at critical values of rotational angle  $\theta$ , we refer to this event as "self-contact". At self-contact, we find that  $A_{1,1} = A_{2,2}$  and  $\phi = 0$ . These relations are used to solve for the self-contact rotation  $\theta_{contact}$ . Likewise, the calculations lead to knowledge of the net height of the specimen and thus the self-contact strain  $\varepsilon_{contact}$ . In Supplementary Figure 2(b) the relationship between the self-contact strain  $\varepsilon_{contact}$  and the geometric ratio  $\rho$  of the  $C_2$  unit cell is presented. The strain at contact decreases as the distance between the voids increases. For instance, at  $\rho = 1.6$  a self-contact strain of  $\varepsilon_{contact} = 0.201$  is determined. In this report, all samples fabricated of the  $C_2$  and  $D_1$  unit cells employed a  $\rho = 1.6$  geometric ratio.

#### 4.2 Modal analysis

We undertake a modal analysis of the  $C_2$  unit cell via the finite element method in ABAQUS to illuminate buckling modes that govern connectivity of the sample Ag-TPU traces when the metamaterials are subjected to uniaxial compression. Periodic boundary conditions are imposed

on the lateral boundaries to study nominal unit cell mechanical behavior. As shown in Supplementary Figure 3(a), one buckling mode at a critical uniaxial strain  $\varepsilon_y$  of 0.0279 is determined with two deformation states. The two states of deformation for the lowest order buckling mode for  $C_1$  are termed mode  $1_{(1)}$  and mode  $1_{(2)}$  and have opposing rotational behavior, Supplementary Figure 3(a). An experimental metamaterial sample composed of continuous  $C_2$  unit cells also demonstrates the two deformation states, Supplementary Figure 3(b) and (c).



**Supplementary Figure 3.** (a) Modal analysis of the lowest order buckling mode of the  $C_2$  metamaterial unit cell. Experimental images of a metamaterial assembled from  $C_2$  unit cells exhibiting (b) mode  $1_{(1)}$  and (c) mode  $1_{(2)}$ .

## 5. $D_1$ unit cell analysis

Here we array the  $D_1$  unit cell in three layers to create a metamaterial assembly seen in Supplementary Figure 4(a). The modal analysis uncovers the three lowest order buckling modes with similar values of critical strain at 0.0089, 0.0091, and 0.0092 strain, Supplementary Figure 4(b). Considering the three serially assembled layers of the metamaterial in Supplementary Figure

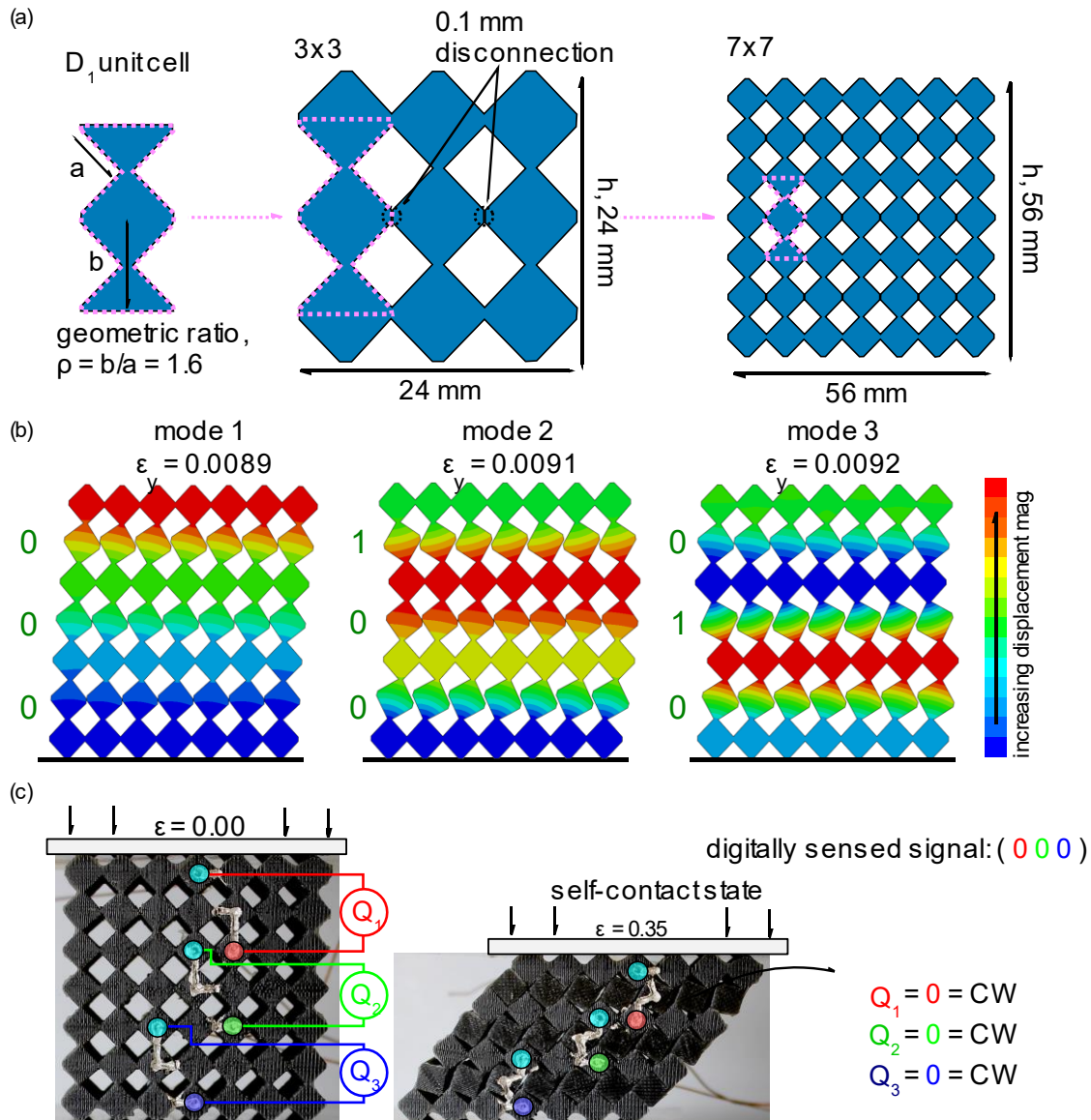


4(a) and the fact that each row may adopt one of two central block rotations, the metamaterial may exhibit at any time 1 of  $(2^3)$  8 deformation states. We adopt the NOT gate elemental circuit utilizing Ag-TPU ink traces to monitor the occurrence of the sample modal response. The undeformed metamaterial assembly is shown in Supplementary Figure 4(c) at left.

Each layer contains inputs and a digital output. One input is a powered input node  $V_{cc}$ , shown as the cyan color highlight in Supplementary Figure 4(c). The digital inputs that govern the logic gate operation are the result of mechanical deformation and thus the rotation of the collapsing layer. Throughout this report, the counterclockwise rotation of the metamaterial unit cell layers corresponds to a digital input of 1, while the clockwise rotation of the unit cells corresponds to digital input of 0. This input notation is selected on the basis of the activation of switching behavior in the fundamental switching component that electrically connects for counterclockwise layer rotation and disconnects for clockwise layer rotation. The same convention is utilized here on the use of the Ag-TPU traces that make up the discrete switching network of electrical connections on the unit cell and metamaterial cross-sections. Alternative conventions and notations may be employed for greater adaptability of digital switching and logic operation based on alternative unit cell mechanical behaviors. As the material is quasi-statically compressed, the digital output Q is monitored at the Ag-TPU trace point shown as the red, green and blue color highlight in Supplementary Figure 4(c) for layer 1, 2 and 3, respectively. An output of 1 or 0 is recorded when the specimen is conductive or nonconductive, respectively.

By utilizing such elementary circuit on the rotational layers of the metamaterial, we develop a method of digital operations to sense the deformation shape of the metamaterial. For instance, at the compact state the system detects a digital output of  $Q_1 = 0$ ,  $Q_2 = 0$ , and  $Q_3 = 0$  that corresponds

to the first buckling mode with a uniform clockwise rotation in all layers. Such investigation illustrates the capability to expand such metamaterial design technique to higher order structures and utilize digital operations for sensing functionalities.



**Supplementary Figure 4.** (a) Schematic of the  $D_1$  unit cell transformation to a  $3 \times 3$  metamaterial, and a  $7 \times 7$  metamaterial. (b) ABAQUS modal analysis results of the  $7 \times 7$  metamaterial. (c) Experimental

**images of the 7x7 metamaterial with Ag-TPU circuit design to detect the deformation states. Depicted in the image is the first buckling mode with a digital output of  $Q_1 = 0$ ,  $Q_2 = 0$ , and  $Q_3 = 0$ .**

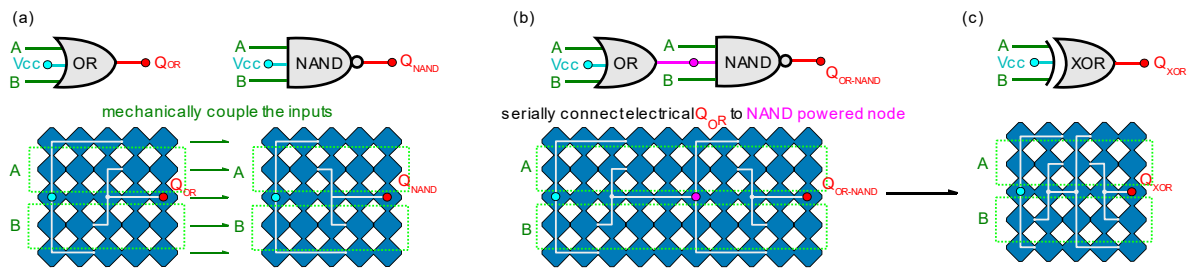
## **6. Logic gate assembly**

The Buffer logic gate Figure 3(d) is the fundamental switch used to formulate all of the metamaterial logic gate. Electrically interfacing the logic gates in series, which is commonly performed in integrated circuits, necessitates a unique approach given the mechanical mode of governing the digital inputs. In this section we discuss three logic gate assembly methods that may be employed for integrated circuit synthesis. Each method is demonstrated using four pairs of logic gate combinations: OR-NAND, NOR-AND, OR-AND, and AND-NAND. These combinations are chosen based on the fundamental Ag-TPU network utilized in each of the gates shown in Figure 4. For instance, the OR gate Figure 4(e) and the NAND gate Figure 4(d) each have two Buffer and/or NOT gates electrically interfaced in parallel. Thus, we combine the gates as OR-NAND to study the outputs of two parallel Ag-TPU networks. The NOR-AND, OR-AND, and AND-NAND are likewise examined below.

### *6.1 Mechanically coupled inputs*

One method of soft, conductive mechanical metamaterial logic gate assembly involves mechanical coupling of the digitized inputs. For instance, Supplementary Figure 5(a) illustrates such method of assembly on an OR and NAND gate by connecting the two metamaterials mechanically in parallel. The result in the continuous metamaterial shown in Supplementary Figure 5(b) that is twice the width dimension of each gate contributor. By serially connecting the electrical output of the OR gate  $Q_{OR}$  to the source  $V_{cc}$  of the NAND gate, we develop a two-input logic computation with a combined electrical output  $Q_{OR-NAND}$ . Interestingly, the electrical output of this particular

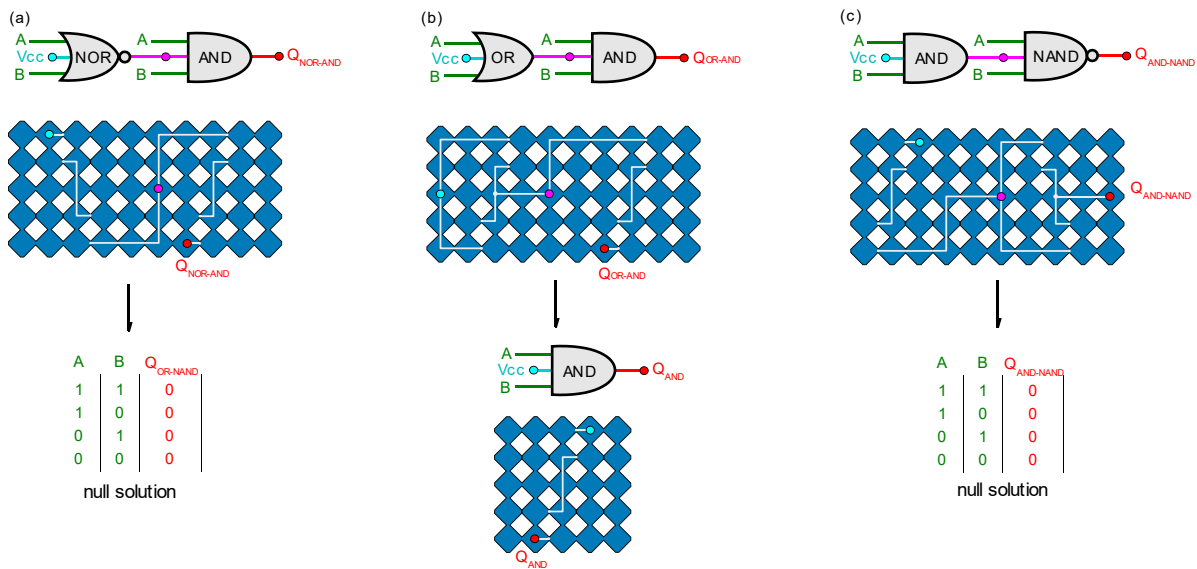
logic gate combination is identical to the output of the XOR gate  $Q_{XOR}$ . In fact, the embodiment of OR-NAND in Supplementary Figure 5(b) may be reduced to the XOR gate shown in Supplementary Figure 5(c). This example shows that by increasing the number of columns that are mechanically stressed in parallel, there are not fundamental changes to the logic gate functionality, which is an important factor in light of scalability of the metamaterial network architecture.



**Supplementary Figure 5. (a) Schematic illustrating the method of mechanically coupling the OR and NAND gate. (b) The OR-NAND logic gate combination through mechanical input coupling. (c) Resulting XOR gate for this OR-NAND combination.**

The schematic in Supplementary Figure 5(b) suggests that mechanical input coupling bears no direct similarity to conventional logic gate networking. As such, there is no way to validate such digital outputs to equivalent, conventional gate combinations. Nevertheless, here we study this gate assembly method for the NOR-AND, OR-AND, and AND-NAND logic gate combinations to characterize the digital output trends. By mechanically coupling the rotational inputs of the NOR and AND gates Supplementary Figure 6(a), a null digital  $Q_{NOR-AND}$  is output. Similar null digital outputs are the result of the AND and NAND combination in Supplementary Figure 6(c). This is an intrinsic limitation of the serial electrical connection approach when the mechanical inputs are coupled. In other words, if the initial logic gate has a digital output of 0, the computational logic

of the second gate is lost due to the absence of the  $V_{cc}$  to the second gate. A second intrinsic limitation to mechanically coupled soft, metamaterial logic gates is observed in the OR-AND combination Supplementary Figure 6(b). For instance, the digital output of the OR-AND  $Q_{OR-AND}$  is identical to that of the AND gate  $Q_{AND}$  and thus the output of OR gate is lost. While these are interesting trends for mechanically coupled metamaterial logic gates, the lack of direct electrical gate analogies limits the utility of this metamaterial logic gate assembly method.

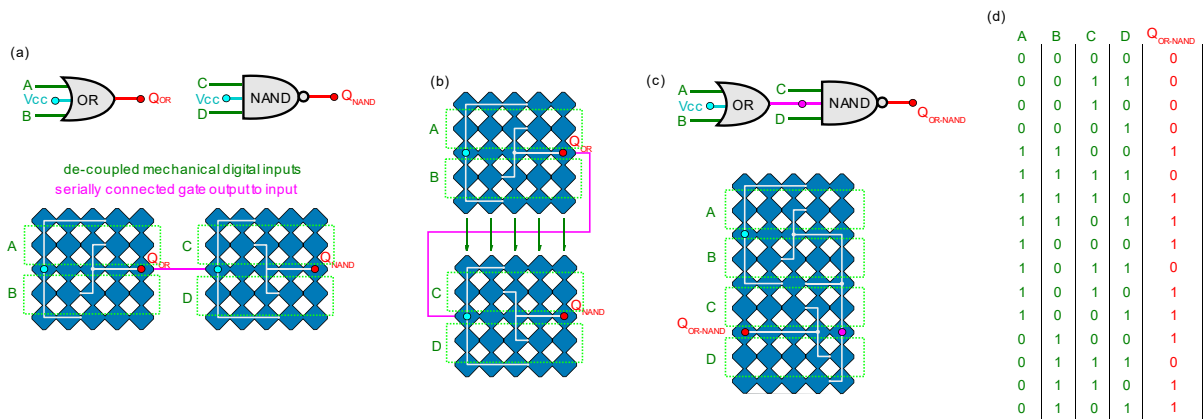


**Supplementary Figure 6. The (a) NOR-AND, (b) OR-AND and (c) AND-NAND logic gate combinations and the resultant truth table or equivalent logic gate.**

## 6.2 Mechanically decoupled inputs

In this method we decouple the mechanical inputs and serially interface the Ag-TPU networks from each of two logic gates. As exemplified in Supplementary Figure 7(a) for the OR-NAND combination, the electrical output  $Q_{OR}$  drives the input  $V_{cc}$  of the NAND gate, while each metamaterial embodiment is structurally separated. This produces 4 mechanical inputs: A and B

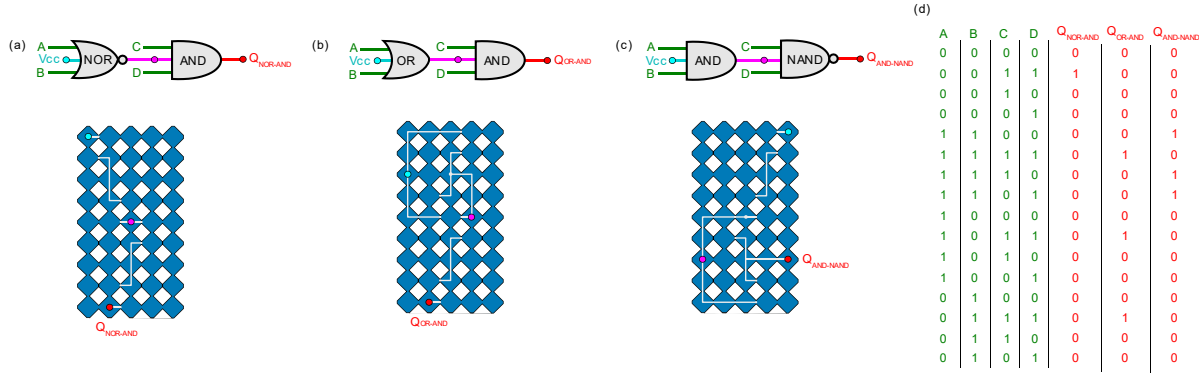
into the OR gate, and C and D into the NAND gate. In fact, this approach is identical to an alternative serial mechanical interface that exploits higher order buckling modes of a continuous metamaterial, Supplementary Figure 7(b). The resultant metamaterial logic gate is shown in Supplementary Figure 7(c). This gate leverages 16 ( $2^4$ ) distinct buckling modes, leading to the  $Q_{OR-NAND}$  truth table in Supplementary Figure 7(d). The digital outputs  $Q_{OR-NAND}$  illustrate a nonconventional logic process without an equivalent electrical gate combination.



**Supplementary Figure 7. Schematic illustrating the method of mechanically decoupled assembly of the OR and NAND gate through (a) mechanical separation or (b) serial mechanical continuity. (c) The OR-NAND logic gate with four mechanical inputs, A, B, C and D. (d) Resultant digital output truth table.**

We examine the NOR-AND, OR-AND, and AND-NAND logic gate combinations using the mechanical decoupling assembly method in Supplementary Figure 8. Each of the gate combinations yields truth table outputs that have no equivalent electrical gate combination due to the fact that the powered  $V_{cc}$  of the second gate is governed by the output of the first gate in the electrical network. As a result, it is not possible to validate the truth tables in Supplementary Figure

8(d). On the other hand, this method leads to non-null digital outputs for all logic gate combinations, unlike the mechanical coupling approach evaluated in Sec. 6.3.



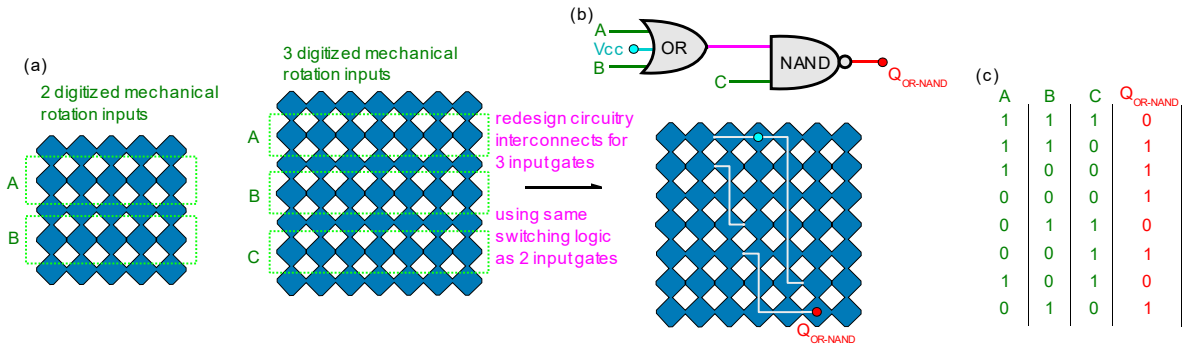
**Supplementary Figure 8. The (a) NOR-AND, (b) OR-AND and (c) AND-NAND logic gate combinations with (d) respective digital output truth tables.**

### 6.3 Mechanical-electrical network synthesis

Here, we study a final method of assembling the soft, conductive mechanical metamaterial logic gates that synthesizes the gate combinations using the principle of serial and parallel electrical networking of the Buffer and NOT logic gate switches. In this way, exact electrical analogues of the resulting metamaterial logic gate combinations are realized.

As shown in Supplementary Figure 9(a), we transform a two-layer metamaterial into a three-layer metamaterial whereby the networking from the two top-most layers A and B are strategically networked to the bottom-most layer C, Supplementary Figure 9(b). A conventional 3 input OR-NAND gate combination is realized by simultaneously considering that both the OR gate Figure 4(e) and the NAND gate Figure 4(d) have two Buffer and/or NOT gates electrically interfaced in parallel. By synthesizing this fact on the basis of the electrical network, we realize the OR-NAND logic gate combination in Supplementary Figure 9(b) that yields a truth table Supplementary

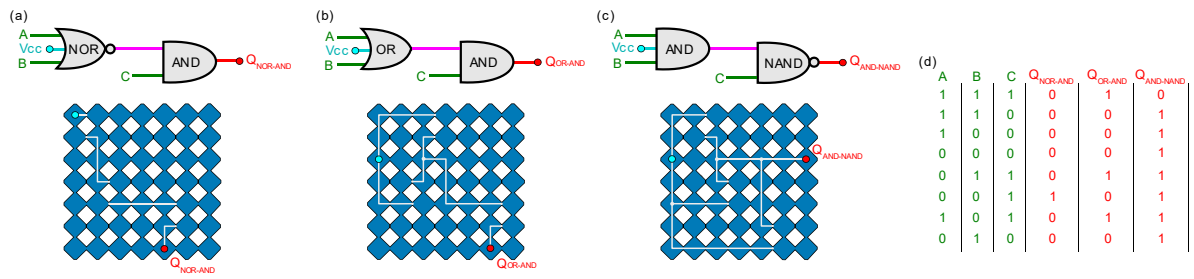
Figure 9(c) in agreement with the electrical analogue. Since there are 3 rotating layers, the metamaterial exhibits 8 ( $2^3$ ) buckling modes that correspond to the digital input combinations permitted by an electrical  $Q_{\text{OR-NAND}}$  logic gate combination.



**Supplementary Figure 9. (a) Schematic illustrating a mechanical-electrical network synthesis approach of metamaterial logic gate combination. (b) The OR-NAND logic gate combination with three mechanical inputs A, B, and C. (c) Resultant digital output truth table.**

We use this strategic logic gate synthesis method to formulate the NOR-AND, OR-AND, and AND-NAND gate combinations in Figure S10. For instance, the NOR-AND Supplementary Figure 10(a) utilizes the NOR circuitry Figure 4(f) on input A and B in series with a single switch (Buffer gate) via mechanical rotation input C. Similar approaches to electrically network the OR gate with the AND gate are employed in Supplementary Figure 10(b) and to network an AND gate with a NAND gate in Supplementary Figure 10(c). The truth tables for these gates in Supplementary Figure 10(d) agree with each of the conventional electrical analogues. Thus, by a synthesis of metamaterial mechanical layering, Ag-TPU networking, and electrical interfaces that accommodate the necessary serial or parallel digital input needs identified from the constituent logic gates in Figure 4 of the main text, one may realize any arbitrary combination of the soft, conductive mechanical metamaterial logic gates.





**Supplementary Figure 10. The (a) NOR-AND, (b) OR-AND and (c) AND-NAND logic gate combinations and (d) respective digital output truth tables.**